ARTICLE   OPEN

Check for updates

Searching for ductile superconducting Heusler X_2YZ compounds

Noah Hoffmann [1], Tiago F. T. Cerqueira [2], Pedro Borlido[2], Antonio Sanna [3], Jonathan Schmidt [1] and Miguel A. L. Marques [1]✉

Heusler compounds attract a great deal of attention from researchers thanks to a wealth of interesting properties, among which is superconductivity. Here we perform an extensive study of the superconducting and elastic properties of the cubic (full-)Heusler family using a mixture of ab initio methods, as well as interpretable and predictive machine-learning models. By analyzing the statistical distributions of these properties and comparing them to anti-perovskites, we recognize universal behaviors that should be common to all conventional superconductors while others turn out to be specific to the material family. In total, we discover a total of eight hypothetical materials with critical temperatures above 10 K to be compared with the current record of $T_c = 4.7$ K in this family. Furthermore, we expect most of these materials to be highly ductile, making them potential candidates for the manufacture of wires and tapes for superconducting magnets.

INTRODUCTION

The image of a superconductor (likely a YBaCuO ceramic) immersed in liquid nitrogen and levitating over an array of magnets is undoubtedly familiar to anyone who has ever witnessed a science demonstration. These ceramics still hold the record for the highest superconducting transition temperature (T_c) at ambient pressure (at around 133 K for $HgBa_2Ca_2Cu_3O_{1+x}$[1]), but other materials with high-T_c have been found in the past decades[2], e.g., MgB_2 ($T_c = 39$ K[3]), fullerides such as Cs_3C_{60} ($T_c = 38$ K[4]), thin films of FeSe ($T_c > 100$ K[5]), etc. More recently, hydrides with exceptionally high critical temperatures were also discovered, but at very high pressure[6].

In spite of these remarkable advances, to this day, niobium-containing materials discovered in the 1950s and 1960s are still the go-to choice for commercial applications[7], the most relevant of which are niobium-titanium (Nb–Ti) alloys. Notably, this happens in spite of their maximum critical temperature of 9.8 K at 24 percent by weight of Ti[8], which pales in comparison with the previous examples. Nb_3Sn is another commercial superconductor, presenting not only a higher critical temperature of 18.5 K but, more importantly, a larger critical field of 30 T[9]. Because of this, it finds use in applications requiring much larger operating magnetic fields than those attainable by Nb–Ti alloys. The prototypical example of this is the operating electromagnets of the International Thermonuclear Experimental Reactor (ITER), where Nb–Ti wirings are supplemented with Nb_3Sn inner windings.

Looking at metrics like critical fields and temperatures alone, it is hard to understand why Nb–Ti has not been entirely replaced by Nb_3Sn (nor by any other high-T_c superconductor) as the industry standard. It is true that these two properties are necessary for a 'good' superconductor, but they are not sufficient from an engineering point-of-view, as a more critical aspect is the ability to draw material into continuous wire or tape several kilometers long with consistent fabrication quality. This, generally speaking, translates into a need for ductile materials. For example, although Nb_3Sn is used in devices, the manufacture of wires is complicated due to its brittleness and requires complex production methods leading to higher fabrication costs[7]. Higher-temperature super-conductors, such as MgB_2 or ceramics, are even more brittle than Nb_3Sn, leading to even more complex manufacturing problems.

Several requirements come to mind in the search for new superconductors that can replace Nb–Ti alloys in commercial applications—ductility, lower density to accommodate easier transportation, higher critical field, no Nb, which is considered a critical raw material by the European Union[10], and compatibility with available production methods. Broadly speaking, these conditions point toward intermetallic compounds (as the presence of non-metallic elements often leads to brittle materials) and first- or second-row metallic elements (where superconductivity is usually driven by the conventional electron-phonon mechanism). These systems can be treated in a straightforward manner by modern ab initio techniques: electron-phonon superconductivity is well understood[2] and several electronic structure packages implementing some form of Eliashberg theory for the calculation of critical temperatures exist. Mechanical properties such as ductility, trivially treated at the macroscopic level, are harder to translate in terms of atomic calculations, but nonetheless, some models are available[11]. Finally, machine-learning methods can be used to accelerate the calculations and to help in the interpretation of the results[12,13].

Studying all intermetallic prototypes is, at the moment, untractable, and thus we will focus on a specific family of compounds, namely the (full-)Heuslers. Named after Fritz Heusler, these are a large class of intermetallic compounds which crystallize in a face-centered cubic structure and have X_2YZ composition, where X and Y are transition metals, and Z is a main group metal[14]. Heuslers possess a wide range of compositions and tunable material properties, making them an ideal family to search for ductile superconductors. They have been researched in areas as diverse as thermal conductivity[15], thermoelectricity[16–18], topological insulators[19,20] and magnetism[21–23].

The first superconducting Heusler compounds, found by Ishikawa et al. in 1982[24], were of the form Pd_2REPb, where RE is

[1]Institut für Physik, Martin-Luther-Universität Halle-Wittenberg, D-06099 Halle, Germany. [2]CFisUC, Department of Physics, University of Coimbra, Rua Larga 3004-516 Coimbra, Portugal. [3]Max-Planck-Institut für Mikrostrukturphysik, Weinberg 2, D-06120 Halle, Germany. ✉email: miguel.marques@physik.uni-halle.de

npj

a rare earth metal. Shortly after, in 1983, Wernick et al. discovered superconductivity in Ni-based systems[25]. Since then, several Heusler compounds have been found to be superconducting[24,26–34]. This even includes compounds with a coexisting magnetic and superconducting state, e.g., Pd_2YbSn or Pd_2ErSn[31]. Up to now, the record T_c belongs to Pd_2YSn with 4.7 K[25], followed by Au_2ScAl with 4.4 K[28]. Unfortunately, the elastic properties of full-Heuslers, even though extensively studied in theory works, are much less explored experimentally (see ref. [36] and references therein), being somewhat easier to find information on the half-Heusler family[36–38].

Here, we perform an extensive study of the superconducting and elastic properties of Heusler materials. These are then compared to a very different family of compounds, specifically the anti-perovskites that some of us studied recently[39]. This is interesting, as many anti-perovskites are also superconducting but contain a non-metallic element (such as C, O, N, etc.). This comparison then allows us to discern between properties specific to the Heusler family from behavior generally present in all electron-phonon-driven superconductors.

The remainder of the work is divided as follows. First, we discuss the two steps of high-throughput calculations (one for the full-Heuslers near the convex hull of stability and another for the remaining full-Heuslers within 200 meV/atom of the hull), accompanied by a general discussion of the distribution of relevant properties (e.g., λ, ω_{log}, or T_c). Due to the number of meta-stable materials, the second step was accelerated with the machine-learning models trained with the results from the first step. For the materials with the best-performing critical temperatures, mechanical properties were calculated in an attempt to find those most likely to be ductile. Lastly, we perform a detailed analysis of the materials that we considered to be the best overall. A flowchart showing these various steps is shown in Supplementary Fig. 1.

RESULTS AND DISCUSSION
High throughput
There are several high-throughput studies of the thermodynamic stability (and other properties) of Heusler compounds[40,41], and ground-state calculations for essentially all compounds of this family can be found in several databases[42–44]. Our present analysis begins with the dataset of ref. [44] from which we selected all compounds that are metallic and that lie on (or very close to) the convex hull of stability, as calculated with the PBE exchange-correlation functional. In order to avoid problems associated with magnetism and superconductivity, only materials with a non-magnetic ground state were considered. This selection resulted in a total of 565 materials, with the full list given as Supplementary Information.

For these systems, the phonon dispersion curves were calculated, which resulted in further removing several entries due to the presence of imaginary modes, resulting in 502 entries. Finally, for the remaining dynamically stable systems, we calculated the electron-phonon mass enhancement parameter, λ, and the logarithm averaged phonon frequency, ω_{log}. From these, the critical temperature, T_c, using McMillan's formula[45], as well as Allen-Dynes' modified formula[46], was computed using a constant value of $\mu^* = 0.1$, as detailed in "Methods". For materials with a McMillan temperature higher than 1 K, we also computed the critical temperature using the isotropic Eliashberg equation[47]. All these values can be found in the Supplementary Information.

At this point, we must notice that several structures that the harmonic approximation at 0 K and 0 GPa predicts to be dynamically unstable are known to be synthesizable at room conditions due to anharmonic and entropic effects. This occurs in several superconducting Heuslers, as reported in Supplementary Table I. Discarding structures with imaginary frequencies may certainly lead to missing some superconductors, but the computational cost associated with including higher-order effects makes the calculations prohibitive for a high-throughput search. As such, at present, we ignore these effects and hope they can be addressed in future work.

With respect to the different approaches for calculating T_c, we see that both McMillan's and Allen-Dynes' underestimate the critical values with respect to the Eliashberg one, although these are nonetheless strongly correlated (see Supplementary Fig. 2). Given that the former two values are considerably simpler to obtain, they are a good quantity to use in high-throughput studies and as input for machine-learning studies. In the following, to avoid confusion and without loss of generality, we thus give preference to $T_c^{McMillan}$ in the discussion of distributions and only refer to the other values in more specific cases.

Histograms for the resulting values of λ, ω_{log} and $T_c^{McMillan}$ obtained with the 4×4×4 set of parameters (see "Methods") are presented in Fig. 1.

The parameter λ follows an asymmetric distribution akin to a Poisson distribution but with a slower decaying tail for large values. With a mean value of 0.30, most Heuslers must be considered to have weak electron-phonon coupling. We found a few compounds with larger values of $\lambda > 1$; however, these are typically due to a strong softening of a phonon mode, indicating a possible dynamical instability of the structure. Compared to the anti-perovskites (mean $\lambda = 0.36$), on average, the Heuslers have a smaller value of λ. This can be explained by the presence of first-row non-metallic elements in the anti-perovskites (like C, N, or O) that have the tendency to form strong covalent bonds.

The distribution of ω_{log} is almost symmetric, a fact translated by the proximity of the mean and median values (190 and 192 K,
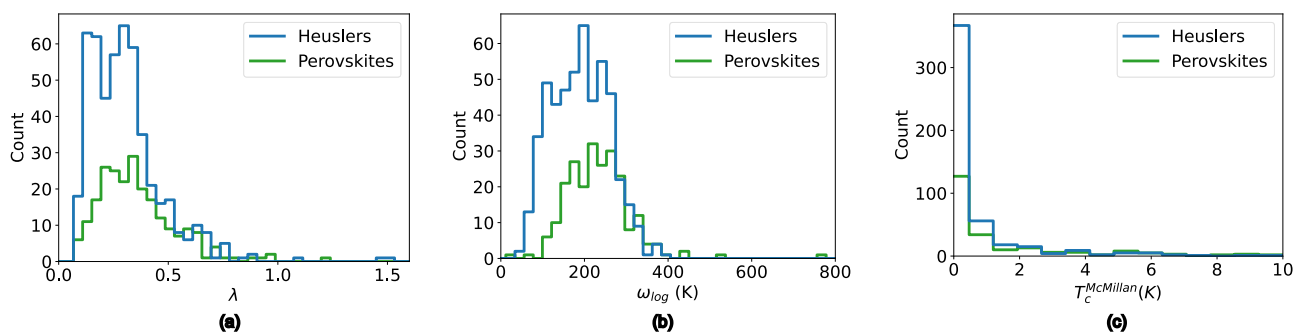

Fig. 1 Histograms of the calculated properties. Histograms of the calculated values (with a 4×4×4 q-point grid) of **a** the electron-phonon mass enhancement parameter λ, **b** the averaged phonon frequency ω_{log} (in K), and **c** the superconducting transition temperature Tc (in K; calculated with the McMillan formula). The blue curves are for Heuslers in our training set, and the green curves are for the anti-perovskites contained in the training set of ref. [39].

respectively), as well as the reduced value of the skewness (0.20). The anti-perovskites show a comparable distribution, at least in qualitative terms. It is also quite symmetric but shifted toward higher values of the frequency range (ω_{log} mean of 234 K, median of 230 K). Given the presence of light elements in the stable anti-perovskites and therefore higher overall phonon frequencies, this was to be expected.

Due to the interplay of factors involved in these two quantities (λ and ω_{log}), they present a loose inverse proportionality relation[2] (see Supplementary Fig. 3). This makes increasing the critical temperature a challenging job since it implies the simultaneous maximization of both parameters. On average, the increased λ of the anti-perovskites with respect to the Heuslers compensates the reduction in ω_{log}, meaning that these materials lie in a higher Pareto front of the (λ, ω_{log}) diagram, and therefore tend to have slightly higher critical temperatures.

Regardless, as seen in Fig. 1, the majority of materials for both families lie in the region below 1 K. Of the handful of outliers with temperatures above 2 K, we find 8 Heusler with $T_c^{Eliashberg}$ above 5 K. The highest of these is Nb_2ReRu for which $T_c^{Eliashberg} = 9.9$ K ($T_c^{McMillan} = 8.3$ K).

Machine learning

The calculations of the previous section are limited to a very thin range of thermodynamic stability. However, meta-stable phases are known to be synthesizable, making them of potential technological interest. Due to the number of materials in this energy range, we opted to accelerate the search by using machine-learning models to screen more efficiently the composition space.

With the data from the electron-phonon calculations, we trained two machine-learning models in an attempt to classify and understand the larger set of materials further from the hull. Our dataset, although large for superconductor standards, is small for the typical use case of machine-learning methods. With this in mind, we chose two models: Operon[48], a framework for symbolic regression, and the model agnostic supervised local explanations (MAPLE)[49]. Besides performing well for smaller datasets, these models have the added benefit of providing some interpretability from the learned model. In the following, we discuss the results from each of the machine-learning models.

Symbolic regression (Operon model). To build an analytical expression for the target properties as a function of the features via symbolic regression, we allowed for the following operators: multiplication, division, a constant, $\log$, $\sqrt{}$, ^{2} and $\exp$. The resulting formulas for each set are presented in Supplementary Tables VI and VII.

For ω_{log} the training of the model yielded the formula

$$\omega_{log} = c_0 + c_1 \cdot \frac{Col_X \, e^{-c_2 \cdot Col_X}}{V} \qquad (1)$$

in four out of the ten different runs, with all runs combined returning a mean absolute cross-validation error of 39.4 K. This formula presents a rather simple dependence on just two quantities: the unit cell volume, V, and the periodic table column of element X, Col_X. The inverse proportionality on V can be understood since large cell volumes usually translate into large atomic radii and therefore larger atomic masses (thus reducing phonon frequencies). As for the column number, a dependence on this quantity is expected from the empirical Matthias' rules[50], modulating a change in number of valence electrons uncorrelated to changes in atomic volumes and masses. It is however curious to notice that Operon finds element X to have a comparatively higher importance than the remaining elements. Equation (1) has a saddle point for $Col_X = 1/c_2$, which for $c_2 \approx 0.2$ (close to the value obtained from all Operon regressions giving this formula) gives a preference for group 5 for atom X.

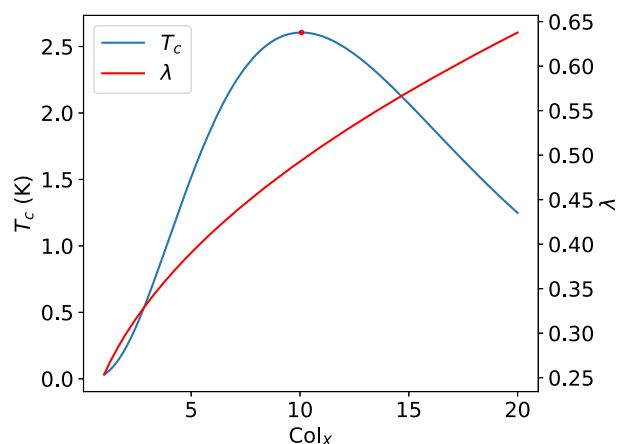For the electron-phonon mass enhancement parameter, the

Fig. 2 **Plot of $T_c(Col_X)$ and $\lambda(Col_X)$ using the equations (2) and (1).** The values for DOS(E_F) and the unit-cell volume were 2.66 (eV/states) and 85 Å^3, which are the mean values of all calculated systems. The red dot indicates the maximum value of T_c.

formula

$$\lambda = c_0 + c_1 \cdot V \sqrt{Col_X \, DOS(E_F)} \qquad (2)$$

appeared in six out of ten runs (and has a mean absolute cross-validation error of 0.114). Independently of the training for ω_{log} a direct dependency on the same quantities was found for λ. The increasing behavior of λ with the density of states is a feature of some models for λ (not necessarily with the sub-linear scaling) and is thus expected. For example, assuming an Einstein solid, the dependence $\lambda \propto DOS(E_F)$ is obtained[51].

Assuming the validity of these formulas for the Heusler family, we can study the evolution of the Allen-Dynes critical temperature formula as a function of the parameters found by Operon (see Fig. 2). Taking V and DOS(E_F) at their mean values, the maximum of T_c is reached for group 10, that contains Ni, Pd, and Pt. This result is in line with previous experimental results, as most known Heusler superconductors with a high T_c do contain Pd.

Random forests (MAPLE model). MAPLE is a random forest-based model capable of accurate predictions while also providing some form of local interpretability. Training the model to predict ω_{log} yields an error of 34 K, better than the error of the Operon formulas. To express the equivalence of the Y and the Z atoms, we can double the data by exchanging their roles, which decreases the error to 27 K. The features with higher weight are the unit-cell volume and the column of the X atom. Additionally, the MAPLE model shows a large weight for the total atomic mass of the compound.

The models for λ have a similar error as the Operon formulas, with a mean absolute cross-validation error of 0.11, regardless of the data doubling procedure. The most important features here are the density of states at the Fermi level, the unit-cell volume and, again, the column of the X atom. Overall, the MAPLE analysis is in agreement with the feature importance returned by the Operon formulas.

With the trained MAPLE model, we are in a position to widen our search of high-T_c Heuslers to materials slightly further from the convex hull. This is interesting as some of these compounds, with relatively small distances to the hull, might still be synthesizable experimentally. Furthermore, extending the number of materials studied gives us a better understanding of the superconductivity of Heuslers and of the extreme values of T_c that are attainable in this family. We therefore listed all compounds below 200 meV $\cdot$ atom^{-1} from the convex hull that MAPLE predicted to have T_c larger than 1 K. As seen from the distribution of the distance to the convex hull available in the Materials Project[52], this threshold
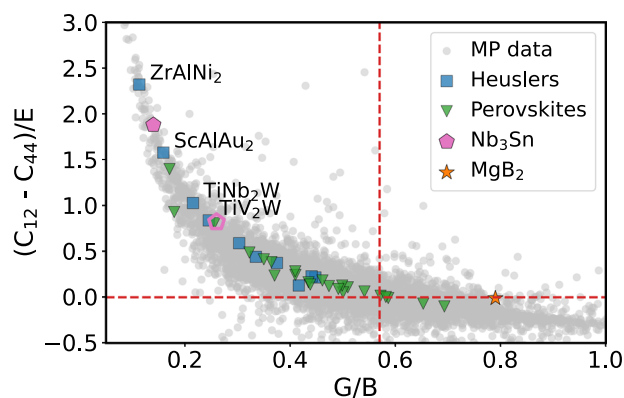
Fig. 3 Dispersion plot of the ductile/brittle classification according to Petiffor's and Pugh's criteria. Green triangles and blue squares represent anti-perovskites and Heuskers, respectively, with $T_c > 5$ K and $E_{hull} < 50$ meV·atom^{-1}. For reference, we also show the calculated values for MgB$_2$ (orange star) and Nb$_3$Sn (pink pentagons). Gray squares represent entries from Materials Project[52]. Due to the considerable error in the theoretical determination of the elastic constants of Nb$_3$Sn, we also show the experimental values from ref. [76] as an empty pentagon.

Fig. 4 Dispersion plot of T_c vs normalized Cauchy pressure, $(C_{12} - C_{44})/E$. Green triangles and blue squares represent anti-perovskites and Heuskers, respectively, with $T_c > 5$ K and $E_{hull} < 50$ meV·atom^{-1}. For reference, we also show the experimental value for Nb$_3$Sn, shown as an empty pentagon.

encompasses the large majority (90%) of the synthesized materials, making it a suitable limit for our search. These 749 materials were then validated by calculating the electron-phonon coupling using the 4×4×4 parameters (see "Methods").

It turns out that the large majority of materials exhibit imaginary frequencies and are dynamically unstable. In fact, this was the case for 641 compounds out of the 749 compounds. A possible explanation for this fact is that MAPLE is predicting materials with very large values of λ that are often dynamically unstable. As expected, the remaining 108 compounds have, on average, higher values of T_c than the training set (see Supplementary Table IV), with the appearance of a noticeable number of materials with temperatures above 5 K and even 10 K.

This shift is also accompanied by a slight qualitative change in the distribution of elements of high T_c materials (see Supplementary Figs. 5 and 6). In the initial training set, a broad distribution of the chemical elements of the periodic table is observed, but with the materials predicted by machine learning, these concentrate around the earlier groups of the transition metals (Ti, V, Cr). The dependence of the mean T_c is much stronger on the column than on the row, in agreement with the results from the machine-learning models. This behavior somewhat contrasts with the distribution of the anti-perovskites, where the distribution is broader, favoring light elements like H, Be and N.

All information regarding these materials is readily available in the Supplementary Information.

Elastic constants and ductility

As the last step of our high-throughput analysis, we now turn to the discussion of the ductility of the superconducting Heuslers. For materials with T_c above 5 K, we computed the stiffness tensor as described in "Methods". From these, we performed the ductility classification as described by Pugh's and Pettifor's criteria for both anti-perovskites and Heuslers. The results can be seen in Figs. 3 and 4, and a complete list is presented in the Supplementary Information. Vickers hardness, H_V, was also estimated using the model from ref. [53]. Models of this type neglect important effects such as grain size, dislocations, etc., which have a notorious effect on hardness. Regardless, they seem to be accurate enough for the present purposes, as we only use them as a comparative proxy for the ductility of the material. Almost all of the materials are classified as ductile using the previous criteria. In addition, most of
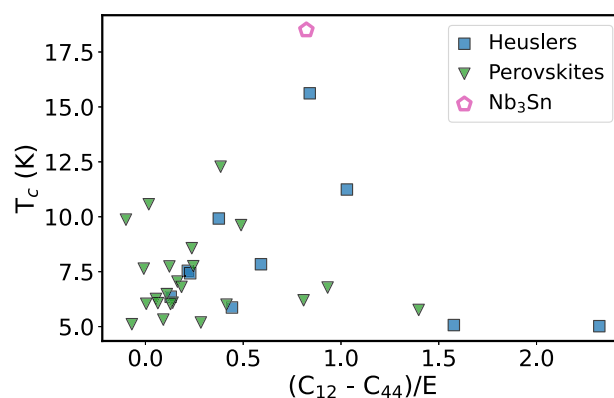
them also have large Poisson ratios, v, and low H_V, further hinting at their ductility.

With respect to anisotropy, we find a rather large range of values for the Zener ratio (A, see Sec. III), from around 0.2 to 4.3. Some extreme cases occur for ZrAlNi$_2$ (for which the extremely low $C_{44} = 10$ GPa, translates simultaneously into low Zener ratio, shear modulus and Pugh's ratio[54]) and LiBe$_2$Pt (where all the constants have comparable magnitudes, but the material still has a comparatively low shear modulus). As for the perovskites, considering the prevalence of elements that are associated with strong covalent (and therefore highly directional) bonds, these are expected to be brittler than the Heuslers, a fact corroborated by the ductility diagram Fig. 3.

Individual entries

Starting from the high-throughput calculations, we selected the 'best' materials within ~50 meV·atom^{-1} from the convex hull for further analysis. These were chosen on the basis of the compromise between critical temperature and ductility. For these materials, more accurate calculations were performed with tighter convergence parameters (see "Methods"). In the following, we discuss a couple of the selected materials, while the complete set of electronic and phononic band structures, along with other superconducting data, is given in the Supplementary Information.

V_2TiMo. This compound has the merit badge of having the highest critical temperature of the present work, with $T_c^{Eliashberg} = 19$ K ($T_c^{McMillan} = 16$ K) and $E_{hull} = 52$ meV·atom^{-1}. However, we must notice that this compound includes vanadium, which is known to lead to strong spin fluctuations[55] (not included in our approach), resulting in a noticeable decrease in T_c.

Looking at the electronic band structure, shown in Fig. 5, although the density of states near the Fermi level is large, it could be slightly increased via hole doping. In turn, this is expected to translate into a small increase of λ and therefore of T_c. This large density of states is due to a series of almost parabolic bands which interpenetrate close to the Fermi level, very similar in shape to that of several other materials here, for example, Ti$_2$NbRe.

In the phonon band structure, we find two notable peaks in the density of states, one close to 170 cm^{-1} and the other one close to 230 cm^{-1}. The former mostly results from V contributions, while the latter is due to both Ti and V in almost equal value. Several phonon branches with strong electron-phonon coupling strength are observed, in particular associated with the two lowest acoustic and optical modes at Γ as well as the lowest frequency modes at L. In total, this gives rise to an electron-phonon mass enhancement
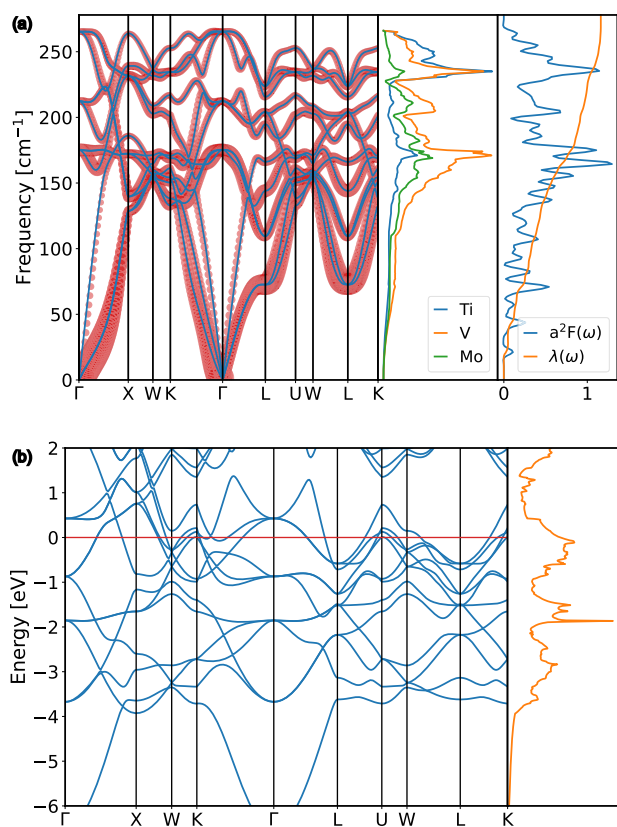
Fig. 5 Calculated phonon dispersion curves and electronic band structure for V₂TiMo. Calculated **a** phonon dispersion curves (along with atom-projected phonon density of states and Eliashberg spectral function) and **b** electronic band structure (along with density of states) for V_2TiMo. Broadening in phonon band structure represents the magnitude of the electron-phonon coupling strength, $\lambda_{n\mathbf{q}}$. Origin of the energy in electronic plots has been shifted to the Fermi level.

Fig. 6 Calculated phonon dispersion curves and electronic band structure for Nb₂TiW. Calculated **a** phonon dispersion curves (along with atom-projected phonon density of states and Eliashberg spectral function) and **b** electronic band structure (along with density of states) for Nb_2TiW. Broadening in phonon band structure represents the magnitude of the electron-phonon coupling strength, $\lambda_{n\mathbf{q}}$. Origin of the energy in electronic plots has been shifted to the Fermi level.

parameter of 1.2. Due to the low density of states at low frequencies, the large $\lambda_{n\mathbf{q}}$ from these modes contribute only moderately to $a^2F(\omega)$ when compared with the aforementioned two peaks. This results in ω_{log} reaching 189 K, which is not particularly large when compared to, for example, Be_2CoNi, but larger than that of Ti_2NbRe.

Elastically, V_2TiMo lies comfortably in the ductile region ($G/B = 0.2$ and $(C_{12} - C_{44})/E = 1.3$). In spite of this, the small value of $C_{44} = 21$ GPa translates into a very small Zener ratio of 0.3, i.e., a highly anisotropic elastic response under shear.

Nb₂TiW. With a lower $T_c^{Eliashberg} = 11$ K ($T_c^{McMillan} = 9$ K), Nb_2TiMo also lies lower in the ductility hyperbole ($G/B = 0.2$ and $(C_{12} - C_{44})/E = 1.0$) with the advantage of being energetically more stable, only 25 meV·atom^{-1} from the hull.

Its electronic structure (see Fig. 6) is remarkably similar to the one of V_2TiMo, showing essentially the same qualitative behavior. The phonon band structure, on the other hand, differs, most notably in the fact that the peak in the density of states due to the contributions of W is shifted to lower frequencies from the peaks of the other elements. Curiously this nonetheless leads to the same value of ω_{log} as V_2TiMo (187 K), but the lower electron-phonon coupling strength leads to the lower λ of 0.8 and, in turn, to the aforementioned lower critical temperature.

Nb₂ReRu. Lower still in the ductility range lies Nb_2ReRu, specifically at $G/B = 0.4$ and $(C_{12} - C_{44})/E = 0.4$. In spite of its position, this material has the small advantage of presenting a much more
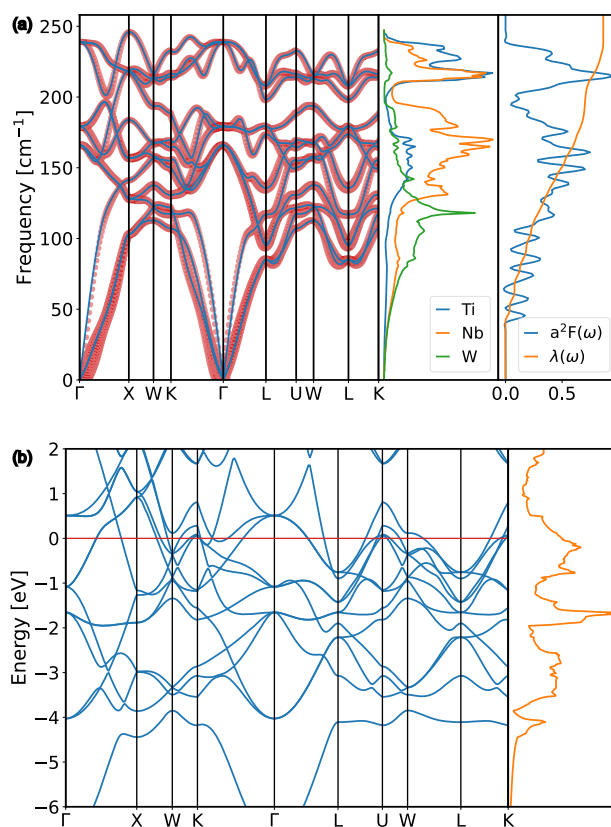
isotropic elastic response than the previous entries ($A = 1$).

Looking at the electronic band structure in Fig. 7, we see that the Fermi level lies in the middle of a 'ramp' in the density of states. Immediately below it lies a sparsely populated energy range due to several band maxima in the neighborhood of the L point, which do not contribute to the Fermi surface. Above the Fermi level, a complicated landscape appears, which ultimately contributes to the large peak circa 0.8 eV. Even if reaching this optimal position is impractical, any level of electron doping would lead to an increase in the density of states at the Fermi level.

The atomic contributions to the phononic band structure are well differentiated, as seen from the corresponding density of states. Below 150 cm^{-1}, the largest contributions come from Ru and Re, with Nb taking over above this point. The modes with the largest $\lambda_{n\mathbf{q}}$ are those close to the L direction, which in spite of the very small corresponding density of states, lead to the largest contributions to $a^2F(\omega)$. Because of this, the value of ω_{log} is low at 190 K and λ at 0.8 is low compared to other top-performing Heusler. As such, we reach the range of $T_c^{Eliashberg}$ of 10 K ($T_c^{McMillan} = 8.3$ K).

In conclusion, we performed a thorough analysis of the superconducting properties of the full Heusler X_2YZ family. These results were then compared to anti-perovskites. Distributions of values of λ, ω_{log}, and T_c have similar shapes in these two families, hinting at the universality of such distributions. Mean values, however, differ due to the different chemistry of both families. As expected from the Heusler family of intermetallics, we observed that the most favorable elements for superconductivity are transition metals, while the anti-perovskites favor the presence of lighter atoms (e.g., H, Be, N), which
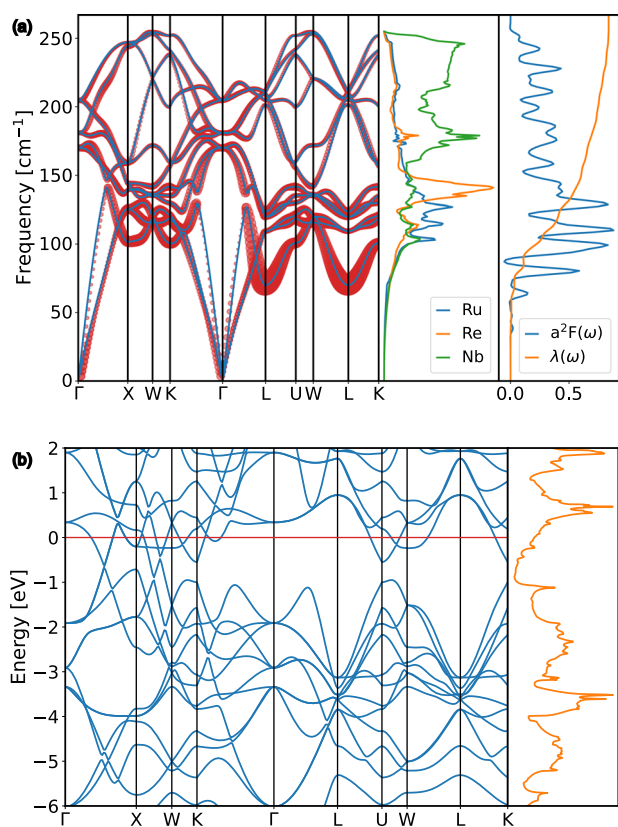
Fig. 7 Calculated phonon dispersion curves and electronic band structure for Nb$_2$ReRu. Calculated **a** phonon dispersion curves (along with atom-projected phonon density of states and Eliashberg spectral function) and **b** electronic band structure (along with density of states) for Nb$_2$ReRu. Broadening in phonon band structure represents the magnitude of the electron-phonon coupling strength, $\lambda_{n\mathbf{q}}$. Origin of the energy in electronic plots has been shifted to the Fermi level.

in turn correlates to higher average phonon frequencies.

As expected, the number of Heusler materials with a critical temperature above 1 K is a small fraction of the total composition space. Regardless, 22 materials were found with critical temperatures above 5 K, and eight of the found materials have critical temperatures above 10 K. This should be compared to the current record of $T_c = 4.7$ K in this family. Furthermore, these materials are expected to be ductile, making them promising for practical applications for the generation of high magnetic fields.

We also show the usefulness of machine-learning models in the interpretation and exploration of the data. Approaches such as symbolic regression and random forests, which perform well for our small datasets, allow us to understand our results and train predictive models.

Further work to include materials in different structural prototypes is now underway and will hopefully lead to more insight into the distribution and the universality of superconducting properties across compound space. Furthermore, increasing the size of the superconducting datasets will lead to more general and accurate machine-learning applications that have the potential to accelerate research in this field.

METHODS
Crystal structure
The starting point for the present work is the crystal structure of Heuslers. This prototype, with chemical composition X$_2$YZ, crystalizes in the $Fm\bar{3}m$ space group (number 225) with the X

Table 1. Convergence of the transition temperature (obtained with McMillan's formula, in K) with respect to the calculation parameters.

Material	3×3×3	4×4×4	6×6×6	8×8×8
AlScAu$_2$	3.51	4.06	4.16	4.15
BeSiOs$_2$	1.77	2.69	1.82	1.82
LiPtBe$_2$	3.53	6.48	4.33	4.31
RuReNb$_2$	9.51	8.69	9.18	9.12

The label corresponds to the number of q-points used.

atoms located at the Wyckoff position $8c(1/4, 1/4, 1/4)$, Y at position $4a(0, 0, 0)$ and Z at $4b(1/2, 1/2, 1/2)$[56,57]. To denote the Heusler compounds, we use the notation X$_2$YZ where Y is the transition metal, and Z is the main group metal[14].

Ground state
Distances to the convex hull within the Perdew-Burke-Ernzerhof (PBE)[58,59] approximation were recalculated with the convex hull of ref.[44]. We note that this hull is considerably larger than the one of the Materials Project[52]. Furthermore, due to the recent updates to the hull[44], some of the compounds that were thermodynamic stable at the beginning of the present work now have positive distances to the convex hull. For completeness, we also present distances to the hull calculated with the PBE for solids[60,61] and SCAN functionals[62] in the Supplementary Information, following the approach and the convex hull of ref.[63].

Electron-phonon
We employed essentially the same workflow and convergence criteria as in our previous work on inverted perovskites[39]. In this way, we could directly compare the two families, as well as accumulate a consistent dataset of superconducting calculations. In short, we performed calculations using QUANTUM ESPRESSO version 6.8 using pseudopotentials from the PSEUDODOJO project[64], specifically the STRINGENT norm-conserving set. We used the high plane-wave cutoff energy as specified in PSEUDODOJO. Self-consistent ground-state calculations were performed with a Gaussian smearing of 0.02 Ry until the energy converged to 10^{-9} Ry. Geometry optimization was stopped when the forces on the atoms were smaller than 10^{-4} Ry/bohr, stresses smaller than 0.05 kbar, and when the difference of energy was smaller than 10^{-5} Ry. The threshold for self-consistency in the phonon calculations was set to 10^{-14} Ry. For the calculation of the superconducting properties, we used the Perdew-Wang[65] local-density approximation. In contrast to ref.[39], we employed the double δ-integration to obtain the Eliashberg function in order to improve the accuracy of the calculations. To select the k- and q-point meshes, we performed convergence tests for four materials (see Table 1). The meaning of the columns is "3×3×3": coarse k-point grid 6×6×6, fine k-point grid 18×18×18, q-point grid 3×3×3; "4×4×4": coarse k-point grid 8×8×8, fine k-point grid 24×24×24, q-point grid 4×4×4; "6×6×6": coarse k-point grid 12×12×12, fine k-point grid 36×36×36, q-point grid 6×6×6; "8×8×8": coarse k-point grid 16×16×16, fine k-point grid 48×48×48, q-point grid 8×8×8. We can clearly see that the 8×8×8 are perfectly converged, while with a 4×4×4 q-grid, one can already obtain a good approximation to T_c. Actually, already with a 3×3×3, results are meaningful. As such, we decided to use the 4×4×4 for the high-throughput search and the 6×6×6 for the systems we discuss in more detail.

Superconductivity
The values of λ, ω_2 and $\omega_{\log}$ (in K) were used to calculate the superconducting transition temperature using the McMillan

formula[45,66]

$$T_c^{McMillan} = \frac{\omega_{log}}{1.20} \exp\left[-1.04\frac{1+\lambda}{\lambda - \mu^*(1+0.62\lambda)}\right],$$ (3)

and the Allen-Dynes modification[46] to it:

$$T_c^{Allen-Dynes} = f_1 f_2 T_c^{McMillan},$$ (4)

where the corrections factor are

$$f_1 = \left\{1 + \left[\frac{\lambda}{2.46(1+3.8\mu^*)}\right]^{3/2}\right\}^{1/3},$$ (5a)

$$f_2 = 1 + \frac{\lambda^2(\omega_2/\omega_{log}-1)}{\lambda^2 + \left[1.82(1+6.3\mu^*)\omega_2/\omega_{log}\right]^2}.$$ (5b)

We arbitrarily took the value of $\mu^* = 0.10$ for all materials studied. We note that this procedure is well-defined for McMillan's and Allen-Dynes' formulas but not for the Eliashberg equations. Indeed, these depend on an extra parameter, the cutoff of the Coulomb interaction, for which we took the (rather arbitrary) value of 0.5 eV.

Elastic constants
In order to study the elastic response of the materials under study, we computed the stiffness tensors via finite differences. Specifically, the elastic constants were obtained by computing the stress of a sufficient set of deformed structures and fitting the resulting values via Hooke's law. This entire procedure was done as implemented in the THERMO_PW package[67]. The underlying calculations were done with QUANTUM ESPRESSO version 6.8 and the Perdew-Wang local-density approximation to the exchange-correlation potential[65]. We resorted to the corresponding STRINGENT set of norm-conserving pseudopotentials from PSEUDO-DOJO[64], from which the largest recommended energy cut-offs were chosen. To assure convergence with respect to the k-point sampling[68], a constant value of 12000 k-points per reciprocal atom[69] was used for all materials.

Due to the directional dependence of the elastic responses, an averaging method is recommended for large-scale analysis. Following the Materials Project, we resort to the Voigt-Reuss-Hill[70–72] average, i.e., the simple average of the higher and lower limits of the response for polycrystalline materials. Anisotropy is another relevant quantity to consider due to the correlation of the different spatial responses with the appearance of failures, such as cracks on crystals under stress. Since in this work, we are dealing with cubic materials, the Zener ratio,

$$A = \frac{2C_{44}}{C_{11}-C_{12}},$$ (6)

is a sufficient quantity to study this. The ratio of the Voigt and Reuss shear moduli also provides a measure of this effect. Both of these quantities are 1 for an isotropic solid, thus giving a simple measure of the anisotropy. Vickers hardness, H_V, was also estimated using the model from ref. [53].

Because of its importance in all areas depending on metallurgy, ductility is well understood at the macroscopic level. However, from an atomistic point-of-view describing ductility is not trivial. Several qualitative models exist based on the type of bonding, but a more attractive approach is models based on elastic properties, readily available from ab initio methods. According to Pugh[54], the ratio G/B (where G is the shear modulus and B the bulk modulus) gives a measure of the brittleness of the material; the smaller the ratio, the more ductile the material. Several works propose different values for the 'critical' ratio defining the onset of brittleness depending on the class of materials under study. The typical value seen in the literature is 0.57, but due to the empirical

nature of the parameter, this value might not be general. A recent work[73] suggests the value 0.44 (Christensen's criterion[74]) as a more realistic threshold for Heuslers. Pettifor's criteria[75] measures the 'directionality' of the bonds via the value of the Cauchy pressure, $C_{12} - C_{44}$, commonly normalized to the Young's modulus, $(C_{12} - C_{44})/E$. Negative values indicate directional bonding associated with brittle behavior. These two criteria can then be used to define a region of interest for ductility.

Machine learning
For each X_2YZ entry, we use as input feature of the models a mixture of structural and atomic properties. For the former, we resorted to the volume of the unit cell (V), density of states at the Fermi level ($DOS(E_F)$) and total atomic weight of the compound (M_{tot}), while for the latter, we used each atom's charge (Q_Λ, where $\Lambda \in \{X, Y, Z\}$), row and column in the periodic table (Row_Λ and Col_Λ), electronegativity (χ_Λ), relative atomic masses ($m_\Lambda = M_\Lambda/M_{tot}$) and covalent radius ($R_\Lambda$). As the atoms Y and Z are equivalent, they were sorted by electronegativity, such that $\chi_Y < \chi_Z$.

Instead of training directly for T_c, we targeted λ and ω_{log} independently in an attempt to minimize errors. Due to the relatively small size of the dataset, we used tenfold cross-validation, randomly splitting the data into a training and validation (in an 80:20 ratio) set. The models were trained in each of the ten independent sets, with the mean of the errors on the corresponding validation sets being the cross-validation error. The several resulting formulas obtained for ω_{log} and λ for the different training sets are presented in the Supplementary Information.

For the symbolic regression with Operon, we allowed for the following operators: multiplication, division, a constant, log, $\sqrt{}$, ^{2} and exp. In the following, we will only mention parameters, which were changed, i.e., any unnamed parameters were left at the default value. We used 100 local iterations, a population size of 2000, 5000 generations. The expression tree was limited to a maximum depth of 10 and a maximum length of 6, and we optimized the mean square error.

MAPLE was used with random forests, 300 estimators, 50% maximum feature participation, a minimum of 10 samples per leaf and a regularization of 0.001.

REFERENCES
1. Schilling, A., Cantoni, M., Guo, J. D. & Ott, H. R. Superconductivity above 130 K in the Hg–Ba–Ca–Cu–O system. Nature 363, 56–58 (1993).
2. Lilia, B. et al. The 2021 room-temperature superconductivity roadmap. J. Phys. Condens. Matter 34, 183002 (2022).
3. Nagamatsu, J., Nakagawa, N., Muranaka, T., Zenitani, Y. & Akimitsu, J. Superconductivity at 39 K in magnesium diboride. Nature 410, 63–64 (2001).
4. Ganin, A. Y. et al. Bulk superconductivity at 38 K in a molecular system. Nat. Mater. 7, 367–371 (2008).
5. Ge, J.-F. et al. Superconductivity above 100 K in single-layer FeSe films on doped SrTiO₃. Nat. Mater. 14, 285–289 (2014).
6. Flores-Livas, J. A. et al. A perspective on conventional high-temperature superconductors at high pressure: methods and materials. Phys. Rep. 856, 1–78 (2020).

7. Narlikar, A. V. *Superconductors* 1st edn (Oxford University Press, 2014).

8. Berlincourt, T. G. & Hake, R. R. Superconductivity at high magnetic fields. *Phys. Rev.* **131**, 140–157 (1963).

9. Dew-Hughes, D. Superconducting A-15 compounds: a review. *Cryogenics* **15**, 435–454 (1975).

10. European Commission. Directorate General for Internal Market, Industry, Entrepreneurship and SMEs. *Report on Critical Raw Materials and the Circular Economy* (European Commission, 2018).

11. Senkov, O. N. & Miracle, D. B. Generalization of intrinsic ductile-to-brittle criteria by Pugh and Pettifor for materials with a cubic crystal structure. *Sci. Rep.* **11**, 4531 (2021).

12. Kulik, H. J. et al. Roadmap on machine learning in electronic structure. *Electron. Struct.* **4**, 023004 (2022).

13. Schmidt, J., Marques, M. R. G., Botti, S. & Marques, M. A. L. Recent advances and applications of machine learning in solid-state materials science. *NPJ Comput. Mater.* **5**, 83 (2019).

14. Bai, Z., Shen, L., Han, G. & Feng, Y. P. Data storage: review of Heusler compounds. *Spin* **02**, 1230006 (2012).

15. Carrete, J., Li, W., Mingo, N., Wang, S. & Curtarolo, S. Finding unprecedentedly low-thermal-conductivity half-Heusler semiconductors via high-throughput materials modeling. *Phys. Rev. X* **4**, 011019 (2014).

16. Carrete, J., Mingo, N., Wang, S. & Curtarolo, S. Nanograined half-Heusler semiconductors as advanced thermoelectrics: an ab initio high-throughput statistical study. *Adv. Funct. Mater.* **24**, 7427–7432 (2014).

17. Raghuvanshi, P. R., Mondal, S. & Bhattacharya, A. A high throughput search for efficient thermoelectric half-Heusler compounds. *J. Mater. Chem. A* **8**, 25187–25197 (2020).

18. Sakurada, S. & Shutoh, N. Effect of Ti substitution on the thermoelectric properties of (Zr,Hf)NiSn half-Heusler compounds. *Appl. Phys. Lett.* **86**, 082105 (2005).

19. Chadov, S. et al. Tunable multifunctional topological insulators in ternary Heusler compounds. *Nat. Mater.* **9**, 541–545 (2010).

20. Lin, H. et al. Half-Heusler ternary compounds as new multifunctional experimental platforms for topological quantum phenomena. *Nat. Mater.* **9**, 546–549 (2010).

21. Kainuma, R. et al. Magnetic-field-induced shape recovery by reverse phase transformation. *Nature* **439**, 957–960 (2006).

22. Krenke, T. et al. Inverse magnetocaloric effect in ferromagnetic Ni–Mn–Sn alloys. *Nat. Mater.* **4**, 450–454 (2005).

23. van Engen, P. G., Buschow, K. H. J., Jongebreur, R. & Erman, M. PtMnSb, a material with very high magneto-optical Kerr effect. *Appl. Phys. Lett.* **42**, 202–204 (1983).

24. Douglass, D. H. (ed.) *Superconductivity in d- and f-Band Metals* (Springer, 1976).

25. Wernick, J., Hull, G., Geballe, T., Bernardini, J. & Waszczak, J. Superconductivity in ternary Heusler intermetallic compounds. *Mater. Lett.* **2**, 90–92 (1983).

26. Klimczuk, T. et al. Superconductivity in the Heusler family of intermetallics. *Phys. Rev. B* **85**, 174505 (2012).

27. Malik, S. K., Umarji, A. M. & Shenoy, G. K. Magnetic and Mössbauer studies on rare-earth-containing Heusler alloys Pd$_2$RSn (R=Tb–Yb). *Phys. Rev. B* **31**, 6971–6975 (1985).

28. Poole, C. P. (ed.) *Handbook of Superconductivity* (Academic Press, 2000).

29. Ramesh Kumar, K., Chunchu, V. & Thamizhavel, A. Van Hove scenario and superconductivity in full Heusler alloy Pd$_2$ZrGa. *J. Appl. Phys.* **113**, 17E155 (2013).

30. Seaman, C. L. et al. Superconductivity and magnetism in the Heusler alloys MPd$_2$Pb (M = rare Earth, Th, and U). *Phys. Rev. B* **53**, 2651–2657 (1996).

31. Shelton, R. N., Hausermann-Berg, L. S., Johnson, M. J., Klavins, P. & Yang, H. D. Coexistence of superconductivity and long-range magnetic order in ErPd$_2$Sn. *Phys. Rev. B* **34**, 199–202 (1986).

32. Waki, S., Yamaguchi, Y. & Mitsugi, K. Superconductivity of Ni$_2$NbX (X = Al, Ga and Sn). *J. Phys. Soc. Jpn.* **54**, 1673–1676 (1985).

33. Winiarski, M. J. et al. MgPd$_2$Sb: a Mg-based Heusler-type superconductor. *Phys. Rev. B* **103**, 214501 (2021).

34. Winterlik, J. et al. Ni-based superconductor: Heusler compound ZrNi$_2$Ga. *Phys. Rev. B* **78**, 184506 (2008).

35. Kierstead, H. A., Dunlap, B. D., Malik, S. K., Umarji, A. M. & Shenoy, G. K. Coexistence of ordered magnetism and superconductivity in Pd$_2$YbSn. *Phys. Rev. B* **32**, 135–138 (1985).

36. Everhart, W. & Newkirk, J. Mechanical properties of Heusler alloys. *Heliyon* **5**, e01578 (2019).

37. He, R. et al. Studies on mechanical properties of thermoelectric materials by nanoindentation. *Phys. Status Solidi A* **212**, 2191–2195 (2015).

38. Rogl, G. et al. Mechanical properties of half-Heusler alloys. *Acta Mater.* **107**, 178–195 (2016).

39. Hoffmann, N., Cerqueira, T. F. T., Schmidt, J. & Marques, M. A. L. Superconductivity in antiperovskites. *NPJ Comput. Mater.* **8**, 150 (2022).

40. Oliynyk, A. O. et al. High-throughput machine-learning-driven synthesis of full-Heusler compounds. *Chem. Mater.* **28**, 7324–7331 (2016).

41. Jiang, S. & Yang, K. Review of high-throughput computational design of Heusler alloys. *J. Alloys Compd.* **867**, 158854 (2021).

42. Curtarolo, S. et al. AFLOWLIB.ORG: a distributed materials properties repository from high-throughput ab initio calculations. *Comput. Mater. Sci.* **58**, 227–235 (2012).

43. Draxl, C. & Scheffler, M. The NOMAD laboratory: from data sharing to artificial intelligence. *J. Phys. Mater.* **2**, 036001 (2019).

44. Schmidt, J. et al. Machine-learning-assisted determination of the global zero-temperature phase diagram of materials. *Adv. Mater.* **35**, 2210788 (2023).

45. McMillan, W. L. Transition temperature of strong-coupled superconductors. *Phys. Rev.* **167**, 331–344 (1968).

46. Allen, P. B. & Dynes, R. C. Transition temperature of strong-coupled superconductors reanalyzed. *Phys. Rev. B* **12**, 905–922 (1975).

47. Allen, P. B. & Mitrović, B. Theory of superconducting tc. *Solid State Phys.* **37**, 1–92 (1983).

48. Burlacu, B., Kronberger, G. & Kommenda, M. Operon C++: an efficient genetic programming framework for symbolic regression. In *Proc. 2020 Genetic and Evolutionary Computation Conference Companion*, 1562–1570 (ACM, 2020).

49. Plumb, G., Molitor, D. & Talwalkar, A. S. Model agnostic supervised local explanations. *Adv. Neural Inf. Process. Syst.* **31**, 2520–2529 (2018).

50. Matthias, B. Superconductivity in the periodic system. *Progress in Low Temperature Physics*, Vol. 2, Ch. 5, 138–150 (Elsevier, 1957).

51. Engelsberg, S. & Schrieffer, J. R. Coupled electron-phonon system. *Phys. Rev.* **131**, 993–1008 (1963).

52. Jain, A. et al. Commentary: The materials project: a materials genome approach to accelerating materials innovation. *APL Mater.* **1**, 011002 (2013).

53. Mazhnik, E. & Oganov, A. R. A model of hardness and fracture toughness of solids. *J. Appl. Phys.* **126**, 125109 (2019).

54. Pugh, S. XCII. Relations between the elastic moduli and the plastic properties of polycrystalline pure metals. *Lond. Edinb. Dublin Philos. Mag. J. Sci.* **45**, 823–843 (1954).

55. Gibson, G. A. & Meservey, R. Evidence for spin fluctuations in vanadium from a tunneling study of fermi-liquid effects. *Phys. Rev. B* **40**, 8705–8713 (1989).

56. Aroyo, M. I., Kirov, A., Capillas, C., Perez-Mato, J. M. & Wondratschek, H. Bilbao Crystallographic Server. II. Representations of crystallographic point groups and space groups. *Acta Cryst.* **62**, 115–128 (2006).

57. Aroyo, M. I. et al. Bilbao Crystallographic Server: I. Databases and crystallographic computing programs. *Z. Kristallogr. Cryst. Mater.* **221**, 15–27 (2006).

58. Perdew, J. P., Burke, K. & Ernzerhof, M. Generalized gradient approximation made simple. *Phys. Rev. Lett.* **77**, 3865–3868 (1996).

59. Perdew, J. P., Burke, K. & Ernzerhof, M. Generalized gradient approximation made simple [Phys. Rev. Lett. 77, 3865 (1996)]. *Phys. Rev. Lett.* **78**, 1396–1396 (1997).

60. Perdew, J. P. et al. Restoring the density-gradient expansion for exchange in solids and surfaces. *Phys. Rev. Lett.* **100**, 136406 (2008).

61. Perdew, J. P. et al. Erratum: Restoring the density-gradient expansion for exchange in solids and surfaces [Phys. Rev. Lett. **100**, 136406 (2008)]. *Phys. Rev. Lett.* **102**, 039902 (2009).

62. Sun, J., Ruzsinszky, A. & Perdew, J. P. Strongly constrained and appropriately normed semilocal density functional. *Phys. Rev. Lett.* **115**, 036402 (2015).

63. Schmidt, J., Wang, H.-C., Cerqueira, T. F. T., Botti, S. & Marques, M. A. L. A dataset of 175k stable and metastable materials calculated with the PBEsol and SCAN functionals. *Sci. Data* **9**, 64 (2022).

64. van Setten, M. et al. The PseudoDojo: training and grading a 85 element optimized norm-conserving pseudopotential table. *Comput. Phys. Commun.* **226**, 39–54 (2018).

65. Perdew, J. P. & Wang, Y. Accurate and simple analytic representation of the electron-gas correlation energy. *Phys. Rev. B* **45**, 13244–13249 (1992).

66. Dynes, R. McMillan's equation and the tc of superconductors. *Solid State Commun.* **10**, 615–618 (1972).

67. Corso, A. D. Elastic constants of beryllium: a first-principles investigation. *J. Phys. Condens. Matter* **28**, 075401 (2016).

68. de Jong, M. et al. Charting the complete elastic properties of inorganic crystalline compounds. *Sci. Data* **2**, 150009 (2015).

69. Ong, S. P. et al. Python Materials Genomics (pymatgen): a robust, open-source Python library for materials analysis. *Comput. Mater. Sci.* **68**, 314–319 (2013).

70. Reuss, A. Calculation of Flow Limits of Mixed Crystals on the Bruus of the Plasticity of Single Crystals. *Z. Angew. Math. Mech.* **9**, 49–58 (1929).

71. Voigt, W. *Lehrbuch der Kristallphysik* (Vieweg+Teubner, 1966).

72. Hill, R. The elastic behaviour of a crystalline aggregate. *Proc. Phys. Soc. A* **65**, 349–354 (1952).

73. Wu, S.-C., Fecher, G. H., Shahab Naghavi, S. & Felser, C. Elastic properties and stability of Heusler compounds: cubic Co$_2$YZ compounds with $I2_1$ structure. *J. Appl. Phys.* **125**, 082523 (2019).

74. Christensen, R. M. *The Theory of Materials Failure* (Oxford University Press, 2013).

75. Pettifor, D. G. Theoretical predictions of structure and related properties of intermetallics. *Mater. Sci. Technol.* **8**, 345–349 (1992).
76. Carroll, K. J. Elastic constants of niobium from 4.2 to 300 K. *J. Appl. Phys.* **36**, 3689–3690 (1965).

ACKNOWLEDGEMENTS

AUTHOR CONTRIBUTIONS

T.F.T.C., P.B and M.A.L.M. performed the ab initio calculations. N.H. and J.S. trained the machine-learning models. A.S. developed the Eliashberg solver. All authors contributed to designing the research, interpreting the results and writing the manuscript.

FUNDING

COMPETING INTERESTS

The authors declare no competing interests.

ADDITIONAL INFORMATION

Supplementary information The online version contains supplementary material available at https://doi.org/10.1038/s41524-023-01084-7.

Correspondence and requests for materials should be addressed to Miguel A. L. Marques.

Reprints and permission information is available at http://www.nature.com/reprints

Publisher's note Springer Nature remains neutral with regard to jurisdictional claims in published maps and institutional affiliations.